

Engineering the electronic structure of single atom Ru sites via compressive strain boosts acidic water oxidation electrocatalysis

Yancai Yao^{1,10}, Sulei Hu^{1,10}, Wenxing Chen^{1,2,10}, Zheng-Qing Huang^{1,3}, Weichen Wei¹, Tao Yao^{1,4}, Ruirui Liu⁵, Ketao Zang⁵, Xiaoqian Wang¹, Geng Wu¹, Wenjuan Yuan⁵, Tongwei Yuan⁶, Baiquan Zhu¹, Wei Liu¹, Zhijun Li¹, Dongsheng He¹, Zhenggang Xue¹, Yu Wang⁷, Xusheng Zheng⁴, Juncai Dong^{1,8}, Chun-Ran Chang^{1,3}, Yanxia Chen¹, Xun Hong¹, Jun Luo⁵, Shiqiang Wei^{1,4}, Wei-Xue Li^{1,*}, Peter Strasser⁹, Yuen Wu^{1,*} and Yadong Li²

Single-atom precious metal catalysts hold the promise of perfect atom utilization, yet control of their activity and stability remains challenging. Here we show that engineering the electronic structure of atomically dispersed Ru₁ on metal supports via compressive strain boosts the kinetically sluggish electrocatalytic oxygen evolution reaction (OER), and mitigates the degradation of Ru-based electrocatalysts in an acidic electrolyte. We construct a series of alloy-supported Ru₁ using different PtCu alloys through sequential acid etching and electrochemical leaching, and find a volcano relation between OER activity and the lattice constant of the PtCu alloys. Our best catalyst, Ru₁-Pt₃Cu, delivers 90 mV lower overpotential to reach a current density of 10 mA cm⁻², and an order of magnitude longer lifetime over that of commercial RuO₂. Density functional theory investigations reveal that the compressive strain of the Pt_{skin} shell engineers the electronic structure of the Ru₁, allowing optimized binding of oxygen species and better resistance to over-oxidation and dissolution.

By developing efficient and durable electrolyzers for water splitting, the intermittent electrical energy generated from renewable wind and solar energy can largely be converted into fuels¹. Water electrolysis using a polymer electrolyte membrane (PEM), based on proton transfer², has been demonstrated to effectively mitigate the drawbacks of an alkaline environment, including the crossover of product gases, limited current density and low operating pressure^{3–5}. Unfortunately, the sluggish catalysed oxygen evolution reaction (OER) and intense degradation of the catalysts^{6,7} in low pH and the strong oxidative environment impeded the widespread adoption of practical electrolyzers⁸. Compared with Ir-based systems, which have better dissolution resistance^{9,10}, Ru has more abundant reserves and has been evaluated to be a more active OER catalyst due to its lower overpotential^{11,12}. The high activity of Ru-based catalysts for the OER in acidic conditions has been linked to its flexible redox state¹³ due to the wide modulation spacing in response to the change in valence state induced by the frequent adsorption/desorption of oxygenated species¹⁴. This was corroborated by the simultaneous emergence of high-valence Ru species and corresponding high OER activity^{15,16}. The moderate oxygen bonding on Ru and low oxygen bulk diffusivity also contribute to its OER activity¹⁷.

Typically, transient dissolution arising from structural disturbance related to frequent changes in the redox state of metals is

responsible for their degradation¹¹. This path is linked to the adsorbate evolution mechanism (AEM) of molecular oxygen generation. However, the accompanying over-oxidation of Ru to Ru-O_x moieties during the generation of (H)O ligands as a result of the demanding oxidative environment under electrode potentials is believed to trigger another dissolution route, where active oxygen-coordinated Ru moieties peel off from defects¹⁸. This represents a primary bottleneck hindering the application of Ru-based catalysts¹⁵. As shown in Supplementary Fig. 1, these defects are mainly oxygen vacancies arising from the oxidative release of lattice oxygen to form molecular oxygen (the so-called lattice oxygen evolution reaction, LOER)^{19,20}. In this dominant dissolution mechanism, as a result of the LOER process, the easy insertion/removal of oxygen in and out of its lattice is significant^{21,22}. Indeed, this rationalizes why thermally synthesized RuO₂, with its better crystallinity and fewer defects^{23,24}, has a lower dissolution rate than electrochemically prepared RuO₂ (refs. 16,22). The rational design of a highly efficient and dissolution-resistant Ru-based OER catalyst requires precise control over the electronic structure of Ru, preventing the dissolution of active Ru species in acid electrolytes and further lowering the overpotential for final industrial applications.

A reasonable means with which to lower the contribution of the LOER to the dissolution of Ru may involve switching the dominant

¹School of Chemistry and Materials Science, iChEM, CAS Center for Excellence in Nanoscience, University of Science and Technology of China, Hefei National Laboratory for Physical Sciences at the Microscale, Hefei, China. ²Department of Chemistry, Tsinghua University, Beijing, China. ³Institute of Industrial Catalysis, School of Chemical Engineering and Technology, Xi'an Jiaotong University, Xi'an, China. ⁴National Synchrotron Radiation Laboratory, University of Science and Technology of China, Hefei, China. ⁵Center for Electron Microscopy TUT-FEI Joint Laboratory Institute for New Energy Materials & Low-Carbon Technologies School of Materials Science and Engineering, Tianjin University of Technology, Tianjin, China. ⁶NEST Lab, Department of chemistry, College of Science, Shanghai University, Shanghai, China. ⁷Shanghai Synchrotron Radiation Facilities, Shanghai Institute of Applied Physics, Chinese Academy of Science, Shanghai, China. ⁸Beijing Synchrotron Radiation Facility, Institute of High Energy Physics, Chinese Academy of Sciences, Beijing, China. ⁹Department of Chemistry, Technical University Berlin, Berlin, Germany. ¹⁰These authors contributed equally: Yancai Yao, Sulei Hu, Wenxing Chen. *e-mail: wxli70@ustc.edu.cn; yuenwu@ustc.edu.cn

O₂ generation mechanism from the LOER to the AEM²⁴. This can be implemented by impeding the fast bulk diffusion rates and surface exchange kinetics of atomic oxygen by changing the coordination environment of the Ru. Metallic Pt has a significantly lower dissolution rate than Ru due to the relatively weaker oxygen bonding, resulting in a lower contribution of the LOER¹¹. Embedding single atomic Ru into a Pt-rich coordination environment with higher corrosion potential may help improve the dissolution resistance of Ru by suppressing any local over-oxidation of Ru surface atoms. In addition, the atomic isolation of Ru without any formation of Ru–O–Ru oxygen bridging bonds maximizes the effect in modulating the coordination of Ru. Previous studies have shown that electrophilic oxygen ligand holes are induced by cationic lattice defects or low-valence metal ion dopants thanks to there being more covalent bonding, which prevents electrons from being transferred from the Ru/Ir centres to their oxygen ligands²⁵. This mechanism will also help keep the resultant surface-exposed Ru sites in lower redox states, given the relatively lower valence state of Pt than Ru^{15,26}. A huge improvement in the isolated Ru's OER activity with the AEM mechanism, without compromising its stability, is further required, due to the failure of the traditional PtRu alloy in the OER activity²⁷. The thin Pt shell environment, subject to compressive surface strain induced by the lattice mismatch, makes this possible^{28,29}. The magnitude of this strain can be controlled by the lattice parameter of the underlying substrate³⁰, through electrochemical leaching or acid etching of the Pt-based alloy. We consider it feasible that single Ru atoms anchored onto strained Pt overlayers may offer a method to efficiently engineer the electronic properties and OER reactivity with respect to redox chemistry.

We have synthesized a series of PtCu_x/Pt_{skin} core–shell structures with atomically dispersed Ru₁ and have unravelled their mechanism of formation, oxidation resistance and the origin of the enhanced OER catalysis by exhaustively examining their structures, coordination environments and oxidation states. Through sequential acid etching and electrochemical leaching, the structure of PtCu_x alloys can be varied (to give PtCu₃, PtCu and Pt₃Cu), which modulates effectively the OER activity catalysed by the Ru₁. The best catalyst, Ru₁–Pt₃Cu, delivers 220 mV overpotential to achieve a current density of 10 mA cm⁻² for acidic OER, with ten times longer lifetime over commercial RuO₂. We found that there is a volcano-type relation between the OER activity and the lattice constant. We argue that the compressive strain of the Pt_{skin} shell effectively engineers the electronic structure and redox behaviour of single atomic Ru anchored at the corner or step sites of the Pt-rich shell, with optimized binding of oxygen intermediates and better resistance to over-oxidation and dissolution.

Results

Preparation and characterization of Ru₁–Pt₃Cu. Uniform five-fold twinned Cu nanowires with an average diameter of 22 nm were prepared based on a previously established method (Supplementary Fig. 2)³¹. Ru-doped PtCu₃ nano-island chains were then generated epitaxially using electroless galvanic redox replacement in the presence of Pt and Ru ions, resulting in the growth of metallic islands consisting of dispersed Ru atoms embedded in a Cu-rich alloy (Fig. 1a). Island growth occurred largely from the five-fold twin boundaries of the pristine Cu nanowires. Epitaxial growth and the resultant nano-island formation of PtCu₃ from the Cu nanowires were corroborated by the identical atomic stacking mode (interplanar spacing and crystal facet orientation) of the island and the underlying substrate, as determined from aberration corrected high-angle annular dark-field scanning transmission electron microscopy (HAADF–STEM) imaging with sub-ångstrom resolution and fast Fourier transform (FFT) patterns (Supplementary Fig. 3 and Supplementary Note 1). Treatments at elevated temperatures from 433 K to 473 K initiated an alloying process between Pt

domains and the Cu substrate as well as a rearrangement of the individual Ru atoms as dopants. As a result, the formation of ordered alloy phases was observed. The observed preferential growth along the twin boundaries might result from a stronger interface interaction of the defect-rich stepped surfaces of twin boundaries³² compared with the other exposed lateral facets of the Cu nanowire. The narrow width of the twin boundaries of the Cu nanowire appear to effectively prevent a lateral extension of the PtCu₃ islands to other facets, further facilitating the formation of one-dimensional (1D) chains of islands. 3D tomographic reconstructions (Fig. 1b) from the 2D HAADF–STEM images clearly demonstrate the preferential growth of Ru domains along the five-fold twin boundaries of the Cu nanowire and the distribution of periodic Pt–Cu islands. More detailed information about the individual Ru, Pt and Cu tomographic images and animated voxel recordings of the rotation of the tomogram are available in Supplementary Video 1, Supplementary Fig. 4 and Supplementary Note 2.

To remove buried non-functional Cu in the bulk of the nanowires as well as non-alloyed Ru, and to provide better accessibility to surface active sites, the Cu nanowires with protruding PtCu₃ nano-island chains were treated in nitric acid. The acid treatment transformed the island chains into an acid-stable Ru-doped PtCu/Pt_{skin} tubular core–shell structure with five-fold rotational symmetry. The core composition transformed thereby from PtCu₃ to PtCu stoichiometry (Fig. 1c), as suggested by the identical interplanar expansion from 0.214 nm (Supplementary Fig. 3e) to 0.218 nm (Fig. 1d) in the nano-islands and underlying substrates. The dissolution of the Cu-rich nanowire core and the Ru–Cu distributed far from twin boundaries was supported further by contraction of the tubular structure diameter from 67 nm (Fig. 1a) to 36 nm (Fig. 1c). The Pt and Ru elemental distribution were retained after the acid etching, according to energy-dispersive X-ray spectroscopy (EDS) elemental mappings (Supplementary Fig. 5), while the absolute Cu content obviously dropped sharply.

The elemental composition of the tubular dealloyed cores and their associated lattice spacing were further modulated by a subsequent electrochemical leaching process brought about by a cyclic voltammetry (CV) scan in N₂-saturated 0.1 M HClO₄ solution (+0.01 V to +1.21 V versus RHE) at a sweep rate of 50 mV s⁻¹. This voltammetric treatment removed additional Cu atoms and formed the final Ru-doped Pt₃Cu/Pt_{skin} core–shell nano-island chains (Supplementary Fig. 6). In essence, the treatment served as an activation procedure for the catalyst. The principle morphology (Fig. 1g) and elemental distribution (Supplementary Fig. 6) of the final nano-island chains were maintained during this CV activation process, although the tubular diameter contracted further from ~36 nm (Fig. 1c) to ~25 nm (Fig. 1g). The core composition (and corresponding interplanar spacing) changed from PtCu (Fig. 1d, 0.218 nm) to Pt₃Cu (Fig. 1h, 0.222 nm). The change in the ratio of Ru, Pt and Cu in three representative samples is shown in Supplementary Table 1. An accurate count of the corner, step and kink defect sites exposed on the nano-island facets revealed that the acid etching and electrochemical leaching had increased the number of surface defects of the nano-island (Fig. 1k), which serve as anchor sites for dispersed individual Ru atoms (Ru₁). The compositional evolution of the alloy core of the tubular catalyst structure from PtCu₃ (green line, Fig. 1k) to PtCu (blue line) after acid treatment and further to Pt₃Cu (red line) after the electrochemical leaching process could be traced by the shift of the face-centred cubic (fcc) X-ray diffraction patterns (XRD) to smaller angles (Fig. 1l). In conclusion, a class of single-atom ternary alloys³³ were synthesized by acid etching and electrochemical leaching.

To further demonstrate the formation of the core–shell structure^{30,34} and atomic dispersion of Ru, atomically resolved elemental mapping³⁵ was performed to provide overall structural information, and typical results of the Pt₃Cu supported Ru are shown in

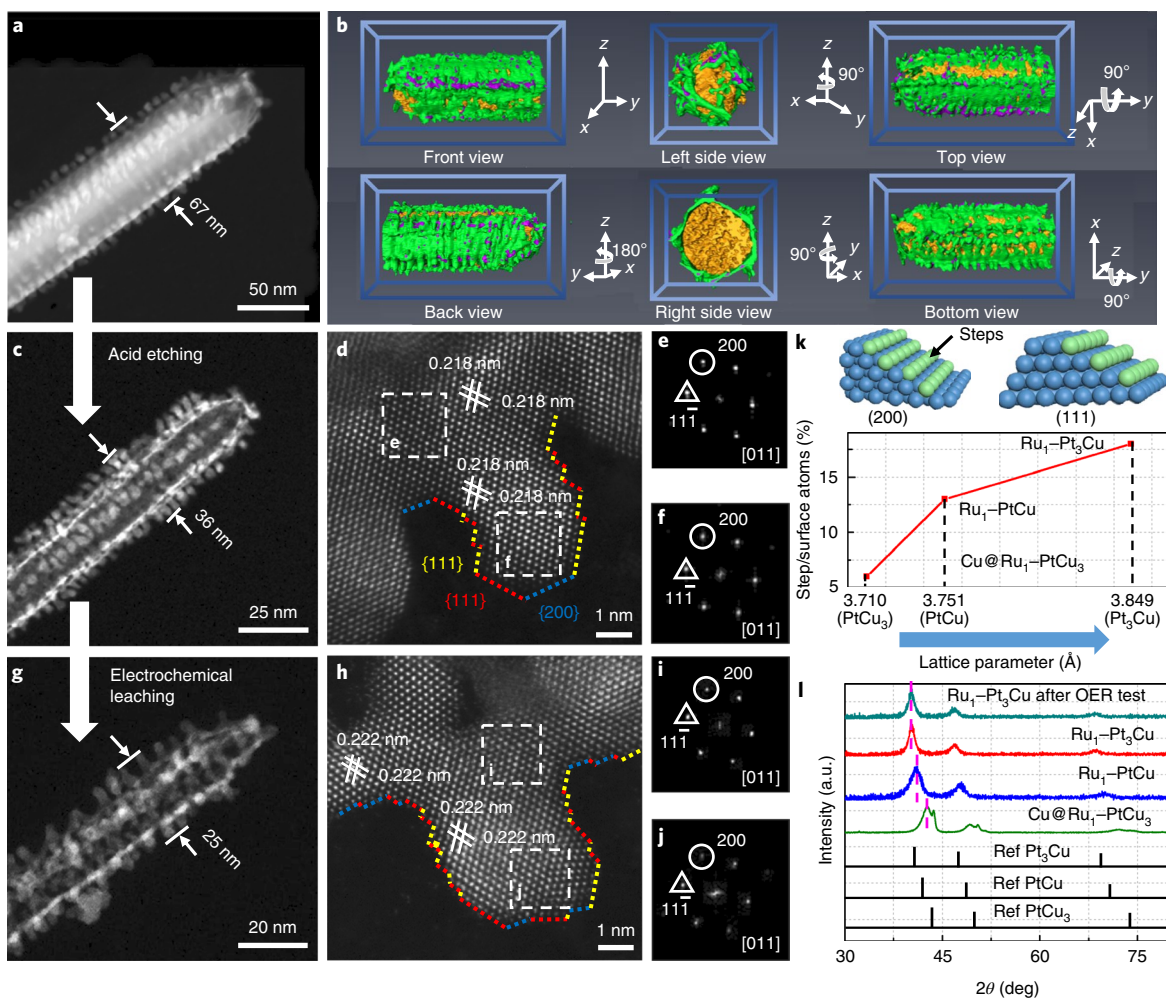


Fig. 1 | Characterizations of $\text{Cu}@Ru_1\text{-PtCu}_3$, $Ru_1\text{-PtCu}$ and $Ru_1\text{-Pt}_3Cu$. **a, b**, HAADF-STEM image (**a**) and six projected images of a three-dimensional visualization of tomographic reconstruction images (**b**) of $\text{Cu}@Ru_1\text{-PtCu}_3$. **c–f**, HAADF-STEM image (**c**), high-magnification image (**d**) and corresponding FFT patterns (**e, f**) of $Ru_1\text{-PtCu}$. **g–j**, HAADF-STEM image (**g**), high-magnification image (**h**) and corresponding FFT patterns (**i, j**) of $Ru_1\text{-Pt}_3Cu$. In **d** and **h**, red and yellow dashed lines represent $\{111\}$ facets and blue dashed lines represent the $\{200\}$ facet. **k**, Statistics of steps exposed on different facets of three representative samples. **l**, XRD spectra of three representative processes.

Fig. 2a–f. Pt-resolved mapping (Fig. 2b) indicated ordered and straight edge structures, which cannot be found in Cu-resolved mapping (Fig. 2c). Superposition of the Pt and Cu mappings (Fig. 2e) showed an ordered atom arrangement and regular geometry profile, which are nearly identical to the corresponding HAADF image (Fig. 2a). The absence of Cu in the topmost layer (red dashed lines in Fig. 2e) provides clearer evidence of the formation of the Pt_{skin} shell. The formation of this Pt_{skin} shell explains the preservation of the XRD peak position (the dark cyan line in Fig. 1l) after 28 h OER test by preventing the bulk diffusion of inner Cu through the Pt_{skin} shell. Finally, negligible variations of the Cu valence state were observed by in situ K-edge X-ray absorption fine structure (XAFS) spectra with increasing working potentials. We believe that this was made possible by separation of the inner Cu species from oxygenated species by the Pt_{skin} shell (Fig. 2g). The Ru elemental distribution in Pt_3Cu shown in Fig. 2d indicates that the Ru is highly atomically dispersed and well separated in the $\text{Pt}_3Cu/\text{Pt}_{\text{skin}}$ matrix, as marked by the arrows in Fig. 2f and Supplementary Fig. 7.

The way in which the atomic isolation and control of the redox state of Ru_1 influence the OER mechanism was further analysed by clarifying its local coordination, using ex situ and in situ XAFS studies at the Pt and Ru edge. The Fourier transform (FT)

of extended XAFS (FT-EXAFS) oscillations (Supplementary Fig. 8 and Supplementary Note 3) revealed that the Ru-doped Pt_3Cu exhibits its one Fourier transform peak located at 1.58 \AA attributed to the scattering of the Ru–O bond, while the peaks at 2.30 \AA and 2.73 \AA are attributed to the Ru–Pt and Ru–Cu bonds (Fig. 2h; for details see Supplementary Figs. 9–11 and Supplementary Tables 2–4). The absence of Ru–Ru bonds (at 2.38 \AA) and related Ru–O–Ru coordination at a higher coordination shell excludes the presence of metallic Ru clusters and RuO_2 particles. This further supports the atomic isolation of Ru species dispersed inside the $\text{Pt}_3Cu/\text{Pt}_{\text{skin}}$ core-shell particles (noted as $Ru_1\text{-Pt}_3Cu$ henceforth). X-ray absorption near-edge structure (XANES) measurements showed that the corresponding Ru K-edge adsorption threshold of $Ru_1\text{-Pt}_3Cu$ locates between the Ru foil and RuO_2 bulk (Supplementary Fig. 12), indicating that surface-exposed Ru_1 sites were not over-oxidized.

Electrocatalytic performance of $Ru_1\text{-Pt}_3Cu$ towards OER. The OER activities of $Ru_1\text{-PtCu}_3$, $Ru_1\text{-PtCu}$ and $Ru_1\text{-Pt}_3Cu$ supported on active carbon (Supplementary Fig. 13) were evaluated and compared to commercial RuO_2 and IrO_2 (Supplementary Fig. 14) in a conventional three-electrode set-up, with O_2 -saturated 0.1 M HClO_4 aqueous solution as the electrolyte. As revealed by the linear

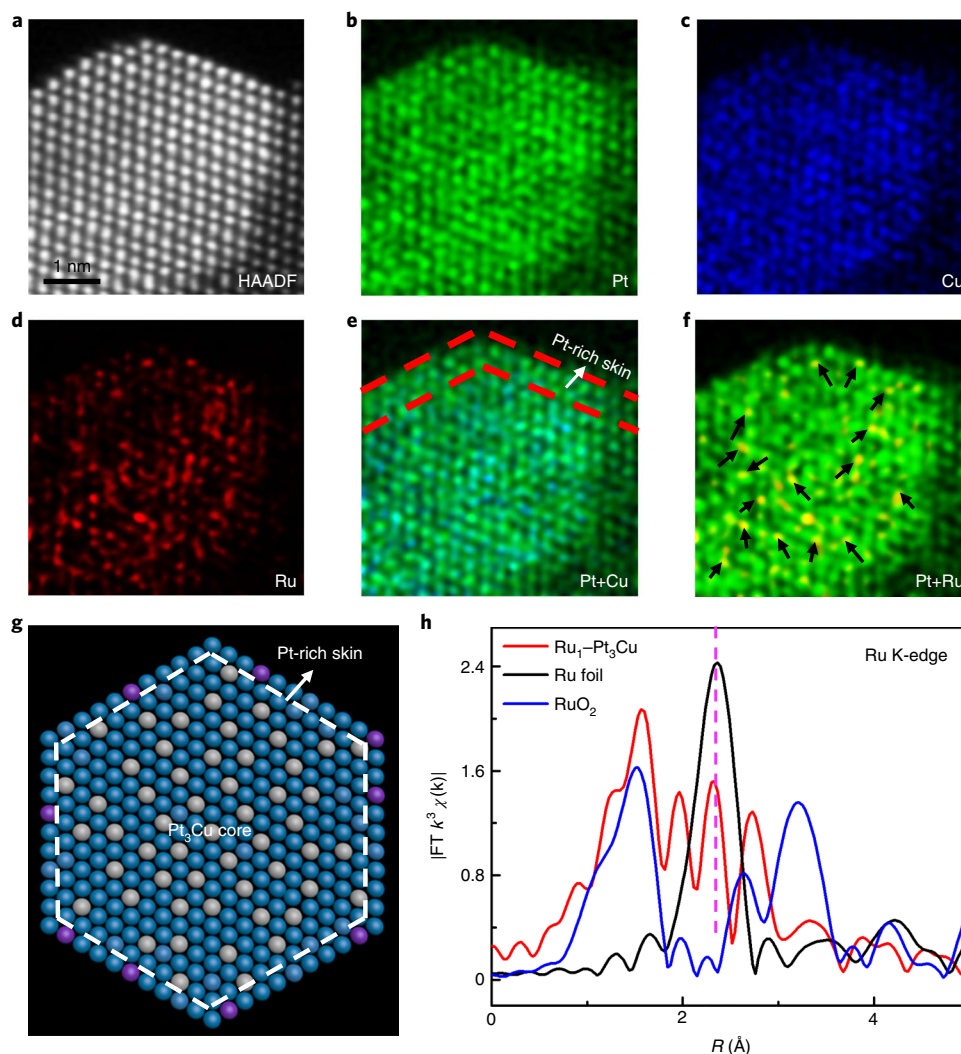


Fig. 2 | Fine-structure characterizations of Ru₁-Pt₃Cu. **a-f**, Atomically resolved elemental mapping of Ru₁-Pt₃Cu. **g**, Schematic atom model of (a). Blue, grey and purple represent Pt, Cu and Ru, respectively. **h**, FT-EXAFS spectra of the Ru K edge.

sweep voltammetry (LSV) presented in Fig. 3a and Supplementary Fig. 15, Ru₁-Pt₃Cu has the catalytically most active polarization curve, with a sharp increase in anodic current density from an onset potential of 1.40 V (potential required to reach 0.1 mA cm⁻²) referred to the reversible hydrogen electrode (RHE). The potential required to reach an OER current density of 10 mA cm⁻² is another key OER performance metric. A 280 mV overpotential was required for Ru₁-PtCu₃ to reach 10 mA cm⁻². With a decrease in Cu ratio, the corresponding overpotential decreased continuously to 250 mV for Ru₁-PtCu and 220 mV for Ru₁-Pt₃Cu. However, for PtRu NPs without any Cu, the corresponding overpotential increased significantly to 340 mV (Fig. 3b and Supplementary Fig. 16). We note that the OER activity of the PtCu alloy was rather poor, with an overpotential of 410 mV (Fig. 3a and Supplementary Fig. 17). This suggests that the atomically dispersed Ru₁ centres embedded in the Pt-Cu alloys act as, or at least participate in, the active site for the OER. To assess the electrochemically active surface area (ECSA) we investigated hydrogen adsorption/desorption during CV as well as CO stripping (Supplementary Figs. 18 and 19 and Supplementary Note 4). The ECSAs calculated from the H_{upd} adsorption/desorption peak area (between 0.05 and 0.35 V) are consistent with the CO stripping results (Supplementary Table 5).

The lattice constants of Ru₁-PtCu₃, Ru₁-PtCu, Ru₁-Pt₃Cu and PtRu NPs are plotted in Fig. 3b. It can be seen that the corresponding lattice constant increased with an increase in the ratio of Pt to Cu, as expected from Vegard's rule³⁶. Interestingly, there is a volcano-type relation between overpotential (lower means more active, hence the volcano is inverse) and the lattice constant. The optimum lattice constant occurred for Ru₁-Pt₃Cu, which will be discussed in detail in the following. To the best of our knowledge, the OER overpotential of Ru₁-Pt₃Cu at the inverse-volcano peak outperformed the state-of-the-art RuO₂ (310 mV) and IrO₂ (380 mV) catalysts in acidic electrolyte (Supplementary Table 6). Due to the atomic dispersion of the active Ru species, Ru₁-Pt₃Cu also shows a remarkable mass activity of 6,615 A g⁻¹ (normalized by Ru) and 779 A g⁻¹ (normalized by Ru + Pt) at η = 280 mV, respectively (Supplementary Fig. 18 and Supplementary Table 7). Polarization curves at different temperatures for Ru₁-Pt₃Cu and RuO₂ were collected to assess the apparent kinetic barriers (Supplementary Fig. 20). The derived Arrhenius plots were extended to the OER thermodynamic equilibrium potential, from which the apparent electrochemical activation energies (E_a) at η = 0 mV could be extracted³⁷. As shown in Supplementary Fig. 21, the extracted E_a for Ru₁-Pt₃Cu was as low as 30.8 kJ mol⁻¹, which is approximately half that of RuO₂ (61.9 kJ mol⁻¹).

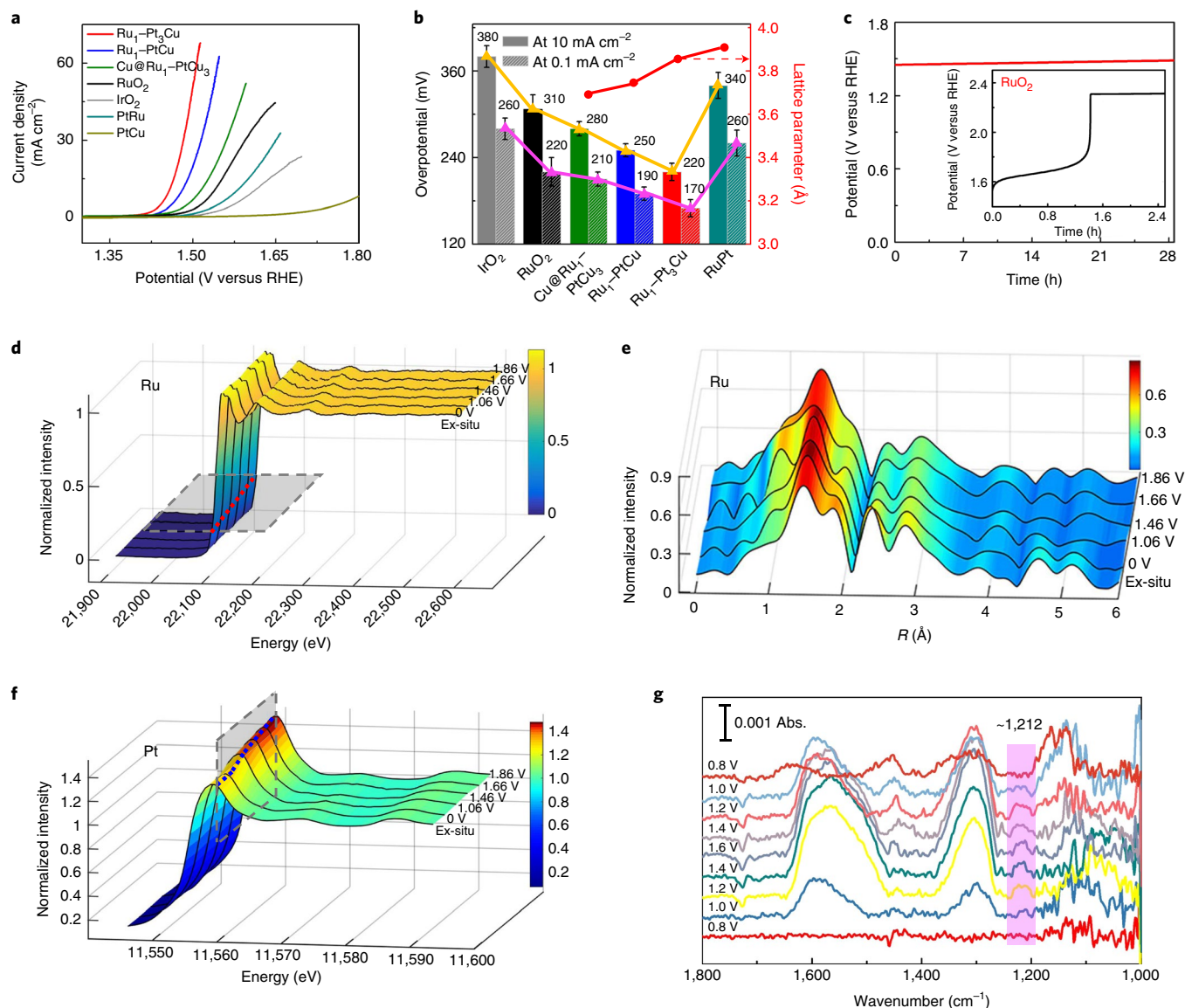


Fig. 3 | Activity and stability investigations of Ru₁-Pt₃Cu during the OER process. **a**, LSV curves of Ru₁-Pt₃Cu, Ru₁-PtCu, Cu@Ru₁-Pt₃Cu and reference samples in an O₂-saturated 0.1 M HClO₄ aqueous solution with 1,600 r.p.m. **b**, Overpotential to reach 0.1 mA cm⁻² and 10 mA cm⁻² for the catalysts (left axis) and lattice parameter dependence on the composition of Pt/Cu (right axis, red line). Error bars show the s.d. evaluated from five independent measurements. **c**, Chronopotentiometric curve obtained with Ru₁-Pt₃Cu and commercial RuO₂ during constant current densities of 10 mA cm⁻². **d-f**, In situ XAFS spectra change of the Ru K-edge (**d,e**) and Pt L₃-edge (**f**). **g**, In situ ATR-IR spectra recorded during the multi-potential steps.

Experiments on a rotating ring-disk electrode (RRDE) showed that the product catalysed by Ru₁-Pt₃Cu were exclusively O₂. This was supported by the oxygen reduction reaction (ORR) polarization curve collected from the ring electrode at a constant disk potential of 1.45 V (Supplementary Fig. 22). When the disk potential varied from 1.27 V to 1.48 V, a negligible current density (<10 μA cm⁻²) assigned to the oxidation of hydrogen peroxide was observed on the ring electrode. According to the ratio of ring and disk currents measured in a separate experiment, the Faradaic efficiency catalysed by Ru₁-Pt₃Cu for OER was as high as 99.8% (Supplementary Fig. 23 and Supplementary Note 5).

The stability of Ru₁-Pt₃Cu and commercial RuO₂ was tested by chronopotentiometry measurements, and the variations in the corresponding potentials are plotted in Fig. 3c. During a 28 h long-term test on Ru₁-Pt₃Cu, the potential required to reach 10 mA cm⁻² was almost constant (decreasing only by 2.1%), well surpassing

that of commercial RuO₂ (inset of Fig. 3c and Supplementary Fig. 24). We also used inductively coupled plasma mass spectrometry (ICP-MS) to quantify the mass loss of Pt, Cu and Ru during *u-t* measurements (Supplementary Fig. 25). The minor dissolved mass of Ru was much lower than the almost 100% dissolution of RuO₂ catalysts under acidic OER conditions after a test lasting approximately 2 h (inset of Fig. 3c). The stability was further demonstrated by the negligible activity decay in the polarization curve after 3,000 cycles (Supplementary Fig. 26). High-resolution transmission electron microscopy analysis on the recycled sample indicated that the island-like morphology and trimetallic interface were preserved to a large extent after the durability test (Supplementary Fig. 27). The great stability of Ru₁-Pt₃Cu might arise from the unique periodic nano-islands providing abundant defect sites that anchor the atomically dispersed Ru₁ and prevent their migration and aggregation.

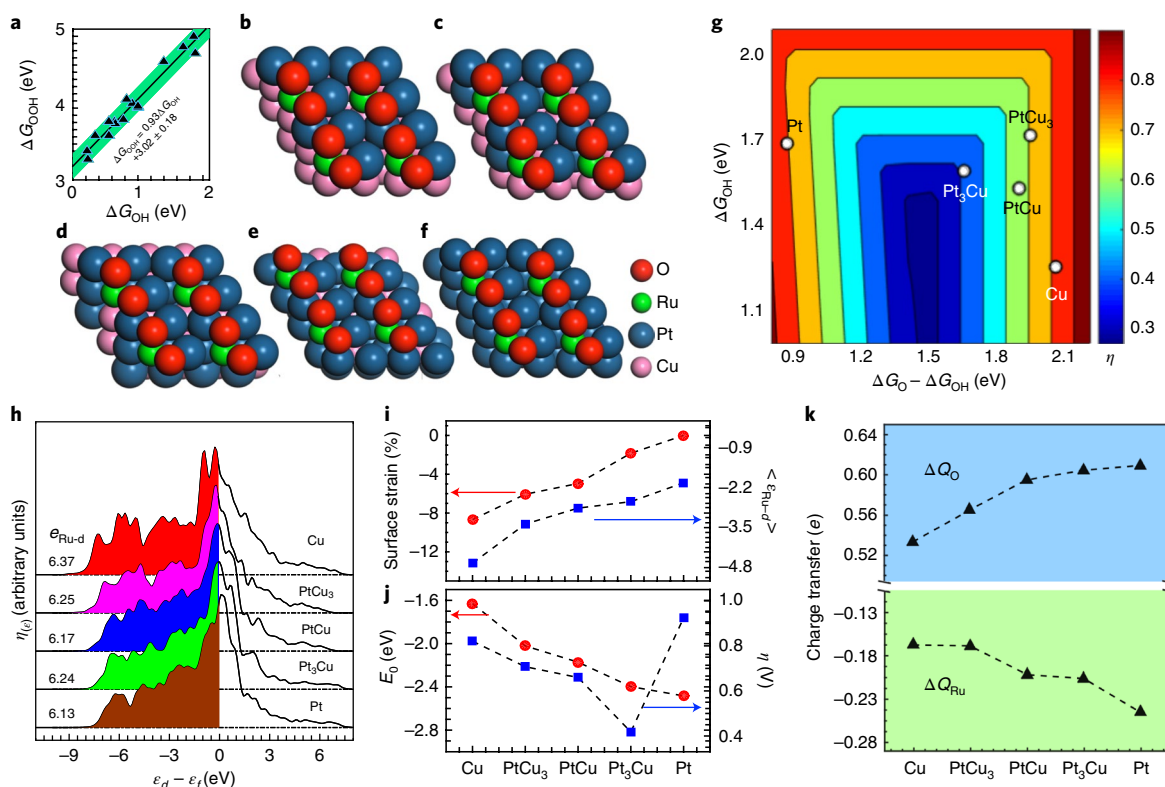


Fig. 4 | Overpotential and electronic structure on Ru₁-Pt_xCu_{4-x}(111) with pre-adsorbed oxygen. **a**, The linear scaling relation between the free energies ΔG of OOH and OH on the alloy surfaces considered. **b–f**, Optimized structures of Cu (111) (**b**), PtCu₃ (111) (**c**), PtCu (111) (**d**), Pt₃Cu (111) (**e**) and Pt (111) (**f**) with surface-embedded Ru₁ atoms and 0.50 ML pre-adsorbed oxygen. **g**, Calculated volcano plot of OER overpotential η with ΔG_{OH} and $\Delta G_{\text{O}} - \Delta G_{\text{OH}}$ as descriptors. **h**, PDOS of surface-embedded Ru₁ 4d with respect to the Fermi level, where $e_{\text{Ru-d}}$ is total 4d electrons of the Ru₁ atom. **i**, In-plane lattice contraction relative to the Pt (111) pristine surface (red circles) and corresponding d -band centre $e_{\text{Ru-d}}$ of Ru₁ (blue squares). **j**, Corresponding adsorption energy E_{O} of the oxygen atoms (red circles) and η (blue squares). **k**, Bader charge ΔQ_{O} for adsorbed oxygen and variation of Bader charge ΔQ_{Ru} for coordinated Ru₁ on alloy surfaces with 0.50 ML pre-adsorbed oxygen.

In situ XAFS and ATR-IR of Ru₁-Pt₃Cu during OER. We carried out in situ XAFS studies to investigate the potential-dependent oxidation of Ru₁ during the OER (Supplementary Fig. 28). With the potential scanned from 0 to 1.86 V, the oxidation state of Ru₁ appeared stable, as shown by the essentially identical Ru₁ K-edge absorption threshold position (Fig. 3d, Supplementary Fig. 29 and Supplementary Note 6) and coordination (Fig. 3e). In contrast, an increase in the white line intensity of the Pt L₃-edge suggests increased d band vacancy for Pt atoms in the Pt–Cu domains (Fig. 3f and Supplementary Figs. 29 and 30), probably because of the electron transferring from Pt to Ru₁. This is further corroborated by X-ray photoelectron spectroscopy (XPS) measurements, which revealed the change in electronic structure at the surface of the catalysts between the initial sample and that after running the chronopotentiometry test (Supplementary Fig. 31 and Supplementary Note 7). Notably, Ru kept the same oxidation state after the u - t measurements, considering the possible charge compensation from Pt–Cu to Ru, thereby avoiding the over-oxidation of Ru. To prove the AEM for the generation of molecule oxygen, we further performed in situ attenuated total reflection infrared (ATR-IR) spectroelectrochemical measurements to capture the OOH intermediate (Fig. 3g and Supplementary Fig. 32). The recorded peak at approximately 1,212 cm⁻¹ is assigned to the characteristic vibration adsorption of the surface-adsorbed superoxide (OOH_{ad})³⁸. This indicates that the AEM rather than the LOER mechanism dominated O₂ generation over the Ru₁-Pt₃Cu, which certainly improved its stability under acidic conditions.

Theoretical insights on OER activity and stability. Density functional theory calculations on various Pt_xCu_{4-x}(111) ($x=0, 1, 2, 3, 4$) surfaces were performed to rationalize the observed activity and dissolution resistance. For the dissolution and segregation of Cu under acidic OER conditions, Pt-skin surfaces³⁹ were used if not stated otherwise, and one-quarter of surface atoms were substituted by Ru to model atomically dispersed Ru₁. Importantly, 0.5 ML oxygen was pre-adsorbed on the surface to simulate the oxidic environment of the Pt_{skin} shell and the Ru atom, as proved by the EXAFS and XANES analyses (Fig. 4b–f). The critical minimum overpotential η , required to enable all OER elementary steps of the OER to be exergonic, was investigated by calculating the free energy profile^{40–42}. Specifically, we calculated the corresponding free energies of OH, O and OOH, the key OER intermediates dominating the overall OER activity. A linear scaling relation between the free energies of OOH and OH on atomically dispersed Ru₁ embedded in the alloy surfaces, $\Delta G_{\text{OOH}} = 0.93\Delta G_{\text{OH}} + 3.02 \pm 0.18$ (Fig. 4a), was found and is in good agreement with previous work¹². Due to the competition between the free energies of the four elementary steps involved⁴³ (Supplementary Fig. 33), the calculated overpotential η can be represented by a 2D volcano-type surface with respect to the free energy of the O and OH intermediates (Fig. 4g). As expected, a too weak binding of adsorbate over the active Ru₁ site (higher ΔG_{OH} and $\Delta G_{\text{O}} - \Delta G_{\text{OH}}$) impedes the adsorption of OH and increases the subsequent dehydrogenation barrier. On the other hand, a too strong interaction (lower ΔG_{OH} and $\Delta G_{\text{O}} - \Delta G_{\text{OH}}$) is detrimental for formation of the OOH intermediate and subsequent generation of O₂. The

best OER activity ($\eta=0.42$ V) close to the peak of the 2D volcano plot was found on the Ru₁-Pt₃Cu (111) (Fig. 4e) surface. In contrast, Ru₁-Cu (111) (Fig. 4b), Ru₁-PtCu₃ (111) (Fig. 4c), Ru₁-PtCu (111) (Fig. 4d) and Ru₁-Pt (111) (Fig. 4f) exhibit overpotentials of 0.82, 0.71 and 0.66 and 0.92 V, respectively, which are less active. Although the trend reproduces the experimental results well, the difference between the calculated (0.42 V) and experimental (0.22 V at 10 mA cm⁻², 0.17 V at 0.1 mA cm⁻²) overpotentials for Ru₁-Pt₃Cu remains, which might arise because of the simplified model used in the calculations.

To shed light on the electronic origin of the computationally predicted beneficial reactivity of atomically dispersed Ru₁, the projected density of states (PDOS) of Ru₁ were analysed and plotted (Fig. 4h). The data reveal that, with an increasing Pt to Cu ratio from PtCu₃, PtCu, Pt₃Cu to Pt, the PDOS of Ru₁ shifts gradually towards the Fermi level, and the corresponding *d*-band centre $\epsilon_{\text{Ru-d}}$ shifts up from -3.37 eV to -2.76 eV. The upshift of the *d*-band centre is understandable because the compressive surface strain with respect to the pristine Pt was gradually released (Fig. 4i). As a result, the oxygen adsorption (E_{O}) is systematically strengthened from -1.63 eV for the pristine Cu (too weak binding) to -2.48 eV for the pristine Pt (too strong binding). This eventually leads to an inverse volcano-type plot of the OER overpotential (Fig. 4j) with respect to the lattice constant, and explains excellently the experimental findings (Fig. 3b).

To rationalize the improved oxidation and dissolution resistance of the Ru₁-Pt₃Cu catalysts observed in the experiments, we used the adsorption of an oxygen atom on various Pt-Cu surfaces with 0.50 ML pre-adsorbed oxygen to probe the corresponding charge transfer (Fig. 4k). It was found that, irrespective of the Pt-Cu surface considered, the adsorbed oxygen gains a considerable amount of charge (~ 0.54 – 0.59 e). However, the coordinated Ru₁ contributes only ~ 0.19 – 0.21 e. This implies that most of electrons gained by the adsorbed oxygen come from the Pt-Cu alloys. Namely, the Pt-Cu alloys could act as an electron reservoir to donate electrons towards reaction intermediates and help prevent the over-oxidation and subsequent dissolution of Ru₁.

Conclusions

In summary, we have synthesized a series of Pt-Cu alloys with embedded Ru atoms as an OER electrocatalyst through acid etching and electrochemical leaching. Atomically resolved elemental mapping revealed that the present Ru species was highly atomically dispersed and the PtCu_x/Pt_{skin} core-shell structure was achieved. In situ XAFS studies demonstrated that the oxidation state of Ru₁ was almost unchanged within the OER catalysis potential range. Accordingly, we have shown how engineering the electronic structure of single Ru sites via compressive strain boosts OER activity by tailoring the binding of oxygenated species close to an optimized level and suppresses its over-oxidation by effectively preventing the electron over-transferring from Ru to the oxygen-containing ligands.

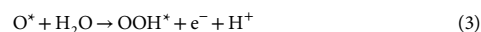
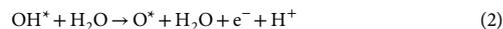
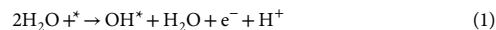
Methods

Theoretical calculations. A series of Pt-Cu bimetal alloys with different crystal phases and stoichiometric, Pt, Pt₃Cu, PtCu, PtCu₃ and Cu, are considered in this work (for their structures, lattice parameters and crystal phases see Supplementary Table 8). To understand the trends we focus only on the (111) surface. All surfaces were modelled as a four-layer slab with layers separated by 15 Å vacuum. To simulate the Pt-skin surface with surface-embedded Ru atoms, the topmost layer was replaced by three-quarters Pt and one-quarter Ru. The atomic coordinates of the optimized structures are provided in Supplementary Data 1.

For all the metal slab models, the bottom two layers were constrained at the bulk position, and the top two layers with adsorbates were fully relaxed. All structures were optimized until the forces on each ion were smaller than 0.02 eV Å⁻¹, and the convergence criterion for the energy was 10⁻⁴ eV. All spin-polarized calculations were performed using the Vienna Ab-initio Simulation Package (VASP)^{44,45}, the Perdew-Burke-Ernzerh (PBE) generalized gradient

approximation (GGA) functional was used for the exchange-correlation potential⁴⁶, and the projected augmented wave (PAW) potential was used to describe the ion-electron interaction⁴⁷. The cutoff energy for the plane-wave basis was set to be 400 eV. All (2 × 2) surfaces were sampled by (6 × 6 × 1) Monkhorst-Pack *k*-point mesh⁴⁸. The total energy of the oxygen molecule was derived from the experimental enthalpy of water and total energy of the water and hydrogen molecule.

At least four elementary steps are usually needed for the OER reaction to proceed, as listed in equations (1) to (4), which involve adsorbed OH, O and OOH species on the surface (*):



As an assessment of the energy change in this process, the Gibbs free energy changes for these four elemental steps can be expressed as

$$\Delta G_1 = \Delta G_{\text{OH}^*} - eU + \Delta G_{\text{H}^+}(\text{pH}) \quad (5)$$

$$\Delta G_2 = \Delta G_{\text{O}^*} - \Delta G_{\text{OH}^*} - eU + \Delta G_{\text{H}^+}(\text{pH}) \quad (6)$$

$$\Delta G_3 = \Delta G_{\text{OOH}^*} - \Delta G_{\text{O}^*} - eU + \Delta G_{\text{H}^+}(\text{pH}) \quad (7)$$

$$\Delta G_4 = 4.92 \text{ [eV]} - \Delta G_{\text{OOH}^*} - \Delta G_{\text{O}^*} - eU + \Delta G_{\text{H}^+}(\text{pH}) \quad (8)$$

where U is the potential measured against the normal hydrogen electrode (NHE) under standard conditions ($T=298.15$ K, $P=1$ bar, $\text{pH}0$). Under these standard conditions, the thermodynamic potential for the oxidation of water to produce oxygen is $\Delta G_{\text{H}_2\text{O}}^{\text{exp}} = 2.46$ V (refs. 49–51). For practical applications, even though only a minimum applied potential of 1.23 V is enough to compensate the increase of thermodynamic energy for every step in the OER reaction (equations (1)–(4)), an additional potential, namely the overpotential η , is always needed to reach a measurable rate for any real electrochemical OER process. The free energy change of the protons caused by non-zero pH can be represented by the Nernst equation as $\Delta G_{\text{H}^+}(\text{pH}) = -k_{\text{B}} T \ln(10) \times \text{pH}$. The total energy change of all these steps will be fixed to 4.92 eV, which is equal to the experimental free energy change to generate two water molecules. The Gibbs free energy differences of these intermediates can be given by $\Delta G_i = \Delta E_i + \Delta \text{ZPE}_i - T\Delta S_i$, where i means OH*, O* and OOH*. Energy differences ΔE_i can be calculated relative to H₂O and H₂ (at $U=0$ and $\text{pH}0$), as given by equations (9)–(11). The zero-point energy (ΔZPE_i) and entropy corrections ($T\Delta S_i$) used in the present work are listed in Supplementary Table 9.

$$\Delta E_{\text{OH}^*} = E(\text{OH}^*) - E^* - \left[E(\text{H}_2\text{O}) - \frac{1}{2} \text{H}_2 \right] \quad (9)$$

$$\Delta E_{\text{O}^*} = E(\text{O}^*) - E^* - [E(\text{H}_2\text{O}) - \text{H}_2] \quad (10)$$

$$\Delta E_{\text{OOH}^*} = E(\text{OOH}^*) - E^* - \left[2E(\text{H}_2\text{O}) - \frac{3}{2} \text{H}_2 \right] \quad (11)$$

The theoretical overpotential is then readily defined as

$$\eta = \max[\Delta G_1, \Delta G_2, \Delta G_3, \Delta G_4] / e - 1.23 \text{ [V]} \quad (12)$$

Characterization. Powder X-ray diffraction patterns of samples were recorded using a Rigaku Miniflex-600 with Cu K α radiation (Cu K α , $\lambda=0.15406$ nm, 40 kV and 15 mA). The morphologies were characterized by TEM (Hitachi-7700, 100 kV). HAADF-STEM images and the corresponding electron energy-loss spectroscopy were collected on a JEOL JEM-ARM200F TEM/STEM with a spherical aberration corrector working at 200 kV.

HAADF-STEM tomography was performed in a FEI Talos F200X operated at 200 kV. The electron micrographs were acquired automatically using a single-axis tilt tomography holder 2021 from -70° to 70° , with projections taken every 1° above 40° , and every 2° below 40° . During acquisition of the HAADF-STEM tilt series, the camera length was 98 mm. Stack alignment and reconstruction of the tilt series were carried out offline using the software package Inspect 3D

4.1.2 (FEI). The aligned tilt series was reconstructed using the Simultaneous Iterative Reconstruction Technique (SIRT)³³ with 100 iterations. The reconstructed structure was segmented manually and visualized in the software package Avizo Version 9.2.0.

Scanning electron microscopy (SEM) was carried out on a JSM-6700F SEM. Nitrogen sorption measurements were conducted using a Micromeritics ASAP 2020 system at 77 K. The XPS experiments were performed at the photoemission end-station at beamline BL10B in the National Synchrotron Radiation Laboratory (NSRL) in Hefei, China. Briefly, the beamline was connected to a bending magnet and covered photon energies from 60 to 1,000 eV with a resolving power ($E/\Delta E$) better than 1,000. In the current work, the structure of the samples were studied at photon energies of 1,253.6 eV. Elemental analysis of Ru, Pt and Cu in the samples was conducted with an Optima 7300 DV for ICP-MS.

Ex situ XAFS measurements. XAFS spectra data (Ru K-edge, Pt L₃-edge and Cu K-edge) were collected at the 1W1B station in the Beijing Synchrotron Radiation Facility (BSRF, operated at 2.5 GeV with a maximum current of 250 mA) and the BL14W1 station in Shanghai Synchrotron Radiation Facility (SSRF, operated at 3.5 GeV with a maximum current of 250 mA). The data were collected at room temperature (25 °C) (Ru K-edge in fluorescence excitation mode using a seven-element Ge detector, Pt L₃-edge in fluorescence excitation mode using a Lytle detector and Cu K-edge in transmission mode using a N₂-filled ionization chamber). All samples were pelleted as disks of 13 mm diameter and 1 mm thickness using graphite powder as a binder.

In situ XAFS measurements. Electrochemical measurements were conducted on a computer-controlled electrochemical analyser (Supplementary Fig. 25). Catalyst-modified carbon paper was used as the working electrode, Pt wire as the counterelectrode and a Ag/AgCl (3 M KCl) electrode as the reference electrode. A home-made electrochemical cell was used for in situ XAFS measurements. In situ XAFS was used to obtain the change of valence state and coordination environment for elemental analysis of the catalyst during reactions. We prepared dilute catalyst solutions (2 mg ml⁻¹ for 5 μl) and distributed them evenly on the centre of carbon paper to form uniform films. The acquired EXAFS data were processed according to standard procedures using the ATHENA module implemented in the IFEFFIT software package. The EXAFS spectra were obtained by subtracting the post-edge background from the overall absorption and then normalizing with respect to the edge-jump step. Subsequently, the $\chi(k)$ data were Fourier-transformed to real (R) space using a Hanning window ($\Delta k = 1.0 \text{ \AA}^{-1}$) to separate the EXAFS contributions from different coordination shells. To obtain the quantitative structural parameters around the central atoms, least-squares curve parameter fitting was performed using the ARTEMIS module of the IFEFFIT software package³³.

The following EXAFS equation was used:

$$\chi(k) = \sum_j \frac{N_j S_0^2 F_j(k)}{k R_j^2} \exp[-2k^2 \sigma_j^2] \exp\left[\frac{-2R_j}{\lambda(k)}\right] \sin[2kR_j + \phi_j(k)] \quad (13)$$

where S_0^2 is the amplitude reduction factor, $F_j(k)$ is the effective curved-wave backscattering amplitude, N_j is the number of neighbours in the j th atomic shell, R_j is the distance between the X-ray absorbing central atom and the atoms in the j th atomic shell (backscatterer), λ is the mean free path (in Å), $\phi_j(k)$ is the phase shift (including the phase shift for each shell and the total central atom phase shift) and σ_j is the Debye–Waller parameter of the j th atomic shell (variation of distances around the average R_j). The functions $F_j(k)$, λ and $\phi_j(k)$ were calculated with the ab initio code FEFF8.2.

The coordination numbers of model samples (Ru foil and RuO₂, Pt foil and PtO₂, Cu foil and CuO) were fixed as nominal values. The obtained S_0^2 was fixed in the subsequent fitting of the Ru K-edge, Pt L₃-edge and Cu K-edge of the samples. The internal atomic distances R , Debye–Waller factor σ^2 and the edge-energy shift ΔE_0 were allowed to run freely.

In situ electrochemical attenuated total reflection Fourier transformed infrared spectroscopy (EC-ATR-FTIRS) measurements. A catalyst ink was first prepared by mixing 1 ml ethanol with 4 mg Ru₁–Pt₃Cu catalyst. The catalyst ink was then dropped via pipette onto a hemicylindrical silicon prism covered with several layers of graphene. A Pt foil and a Ag/AgCl electrode were used as counter- and reference electrodes, respectively. Millipore Milli-Q water (18.2 MΩ cm) and ultrapure perchloric acid (70%, Suprapure, Sigma-Aldrich) were used to prepare the solution. The supporting electrolyte used in the measurement was 0.1 M HClO₄, which was constantly purged with N₂ (5 N, Nanjing Special Gas Corp) during the experiment. Before the experiments, the working electrode was cleaned by continuously scanning the electrode potential in the region 0.6–1.6 V for about 30 min. The electrode potential was held at 0.8 V in 0.1 M HClO₄ and a background spectrum (reflectance R_0) was recorded. The electrode potential was first altered from 0.8 V to 1.6 V stepwise, then back again; in the meantime, infrared spectra

were recorded with a time resolution of 5 s per spectrum at a spectral resolution of 4 cm⁻¹. All spectra were presented as absorbance, $A = -\log(R/R_0)$, where R is the reflectance of the sample spectrum. A Varian FTS 7000e infrared spectrometer with an HgCdTe detector cooled by liquid nitrogen was used.

Preparation of Cu nanowires. In a typical procedure for synthesizing Cu nanowire nanocrystals, CuCl₂·2H₂O (10 mg) and RuCl₃·xH₂O were dissolved in 1 ml ethanol and 3 ml oleylamine. The mixture was sonicated for 30 min. The as-obtained suspension solution was slowly injected into a vial containing 3 ml 1-octadecylene, preheated at 120 °C for 10 min with vigorous stirring, then heated from 120 °C to 160 °C. The reaction last 6 h. After being cooled to room temperature, the products were precipitated by ethanol, separated via centrifugation and further purified by an ethanol–hexane mixture three times.

Preparation of Cu@Ru₁–PtCu₃. In a typical procedure, 5.65 mg of Pt(acac)₂ dissolved in 1 ml oleylamine was added to the as-prepared Cu nanowires and the temperature was changed from 160 °C to 200 °C followed by 12 h thermal treatment at 200 °C. The products were precipitated by ethanol, separated via centrifugation and further purified by an ethanol–hexane mixture several times.

Preparation of Ru₁–PtCu. In a typical procedure to obtain Ru₁–PtCu catalyst, Cu@Ru₁–PtCu₃ nanocrystals were dissolved in 10 ml 7.5 M nitric acid, followed by 2 h stirring at room temperature. Finally, the products were separated via centrifugation and further purified by ethanol.

Preparation of Ru₁–Pt₃Cu. These Ru₁–PtCu nanowires were loaded onto carbon black (XC-72) and annealed in an argon atmosphere at 400 °C for 12 h. The catalysts then underwent CV measurements in N₂-saturated 0.1 M HClO₄ solution (0.01 V to 1.21 V versus RHE) with a sweep rate of 100 mV s⁻¹.

Electrochemical measurements for OER. Electrochemical tests were conducted on a CHI760E electrochemical work station (Chenhua) with a three-electrode system in 0.1 M HClO₄ aqueous solution. The Ag/AgCl (3 M KCl) electrode was used as a reference electrode and a platinum wire was used as a counterelectrode. A constant O₂ or N₂ flow was maintained in the headspace of the electrolyte during the entire experiment. The synthesized Ru₁–Pt₃Cu, Ru₁–PtCu and Cu@Ru₁–PtCu₃, PtRu nanoparticles (NPs) and PtCu NPs were dispersed onto carbon black (Cabot, Vulcan XC-72) with a metal loading of ~30%. The catalysts were subjected to a 400 °C annealing process for 12 h in argon to remove organic surfactants⁵⁴.

The turbid catalyst ink was prepared by mixing 4 mg of the catalyst in 1 ml solution containing 960 μl ethanol and 40 μl 5% Nafion solution, followed by ultrasonication for 30 min. Similarly, the catalyst inks for commercial RuO₂ and IrO₂ samples were prepared by mixing 4 mg in 960 μl ethanol and 40 μl 5% Nafion solution as above.

Next, a certain volume of the catalyst ink was carefully dropped onto a 5-mm-diameter glassy carbon disk electrode or RRDE. The catalyst layer was allowed to dry at room temperature before electrochemical measurements. In 0.1 M HClO₄, the catalyst loading was 0.0163 mg_{Pt+Ru} cm⁻² and the loading of Ru was 0.00192 mg_{Ru} cm⁻² (based on ICP-MS).

Electrochemical impedance spectroscopy measurements were conducted at 1.20 V (versus Ag/AgCl) on a rotation electrode under 1,600 r.p.m. The amplitude of the sinusoidal wave was 5 mV, and the frequency scan range was 100 kHz–0.1 Hz. Unless otherwise stated, all experiments were performed at ambient temperature (25 °C) and all potentials were referenced to the RHE.

CV measurements were carried out in 0.1 M HClO₄ solutions under a flow of N₂ at a sweep rate of 50 mV s⁻¹. The specific ECSA was calculated by measuring the H_{upd} adsorption charge (Q_H) collected in the hydrogen adsorption/desorption region (0.01–0.31 V) after double-layer correction, according to the following relation:

$$\text{ECSA} = \frac{Q_H}{m \times q_H} \quad (14)$$

where Q_H is the charge for H_{upd} (H⁺ + e⁻ = H_{upd}) adsorption, m is the metal loading and q_H (210 μC cm⁻²) is the charge required for monolayer adsorption of hydrogen on Pt surfaces.

For CO stripping, pure CO gas was purged through the catalyst surface in cells filled with 0.5 M H₂SO₄ electrolyte for 30 min while holding the working electrode at 0.1 V (versus RHE). After transferring the electrodes to another cell filled with fresh 0.5 M H₂SO₄ electrolyte (without CO), CO stripping was performed in the potential range 0–1.2 V (versus RHE) at a scan rate of 10 mV s⁻¹. The ECSA_{CO} was also calculated using equation (14).

Rotating disk electrode voltammetry. The electrochemical experiments were conducted in O₂-saturated 0.1 M HClO₄ for the OER at room temperature at 1,600 r.p.m. For RRDE tests, a computer-controlled CHI 760E electrochemical workstation was used, the disk electrode was scanned at a rate of 10 mV s⁻¹ and the ring electrode potential was set to 1.48 V versus RHE. The hydrogen peroxide yield

(H₂O₂%) and the electron transfer number (*n*) were determined by the following equations:

$$\text{H}_2\text{O}_2(\%) = 100 \times \frac{2 \times \frac{I_r}{N}}{I_d + \frac{I_r}{N}} \quad (15)$$

$$n = 4 \times \frac{I_d}{I_d + \frac{I_r}{N}} \quad (16)$$

where *I*_d is the disk current, *I*_r is the ring current and *N*=0.4 is the current collection efficiency of the Pt ring.

The accelerated durability tests of the catalysts were performed in the O₂-saturated 0.1 M HClO₄ electrolyte at room temperature (25 °C) by applying potential cycling between 1.0 and 1.6 V versus Ag/AgCl at a sweep rate of 50 mV s⁻¹ for 3,000 cycles.

Data availability

The data that support the plots within this paper and other findings of this study are available from the corresponding author upon reasonable request.

Received: 15 September 2018; Accepted: 5 February 2019;

Published online: 11 March 2019

References

- Chu, S. & Majumdar, A. Opportunities and challenges for a sustainable energy future. *Nature* **488**, 294–303 (2012).
- Russell, J. H., Nuttall, L. J. & Fickett, A. P. Hydrogen generation by solid polymer electrolyte water electrolysis. *Am. Chem. Soc. Div. Fuel Chem. Prepr.* **18**, 24–40 (1973).
- Kanan, M. W. & Nocera, D. G. In situ formation of an oxygen-evolving catalyst in neutral water containing phosphate and Co²⁺. *Science* **321**, 1072–1075 (2008).
- Vojvodic, A. & Nørskov, J. K. Optimizing perovskites for the water-splitting reaction. *Science* **334**, 1355–1356 (2011).
- Yin, Q. et al. A fast soluble carbon-free molecular water oxidation catalyst based on abundant metals. *Science* **328**, 342–345 (2010).
- Spoeri, C. et al. The stability challenges of oxygen evolving catalysts: towards a common fundamental understanding and mitigation of catalyst degradation. *Angew. Chem. Int. Ed.* **56**, 5994–6021 (2017).
- McCrorry, C. C. et al. Benchmarking hydrogen evolving reaction and oxygen evolving reaction electrocatalysts for solar water splitting devices. *J. Am. Chem. Soc.* **137**, 4347–4357 (2015).
- Carmo, M. et al. A comprehensive review on PEM water electrolysis. *Int. J. Hydrog. Energy* **38**, 4901–4934 (2013).
- Lee, Y. et al. Synthesis and activities of rutile IrO₂ and RuO₂ nanoparticles for oxygen evolution in acid and alkaline solutions. *J. Phys. Chem. Lett.* **3**, 399–404 (2012).
- Stoerzinger, K. A. et al. Orientation-dependent oxygen evolution activities of rutile IrO₂ and RuO₂. *J. Phys. Chem. Lett.* **5**, 1636–1641 (2014).
- Cherevko, S. et al. Dissolution of noble metals during oxygen evolution in acidic media. *ChemCatChem* **6**, 2219–2223 (2014).
- Seh, Z. W. et al. Combining theory and experiment in electrocatalysis: insights into materials design. *Science* **355**, 146–157 (2017).
- Stoerzinger, K. A. et al. The role of Ru redox in pH-dependent oxygen evolution on rutile ruthenium dioxide surfaces. *Chem* **2**, 668–675 (2017).
- Chang, S. H. et al. Activity–stability relationship in the surface electrochemistry of the oxygen evolution reaction. *Faraday Discuss.* **176**, 125–133 (2015).
- Danilovic, N. et al. Activity–stability trends for the oxygen evolution reaction on monometallic oxides in acidic environments. *J. Phys. Chem. Lett.* **5**, 2474–2478 (2014).
- Roy, C. et al. Trends in activity and dissolution on RuO₂ under oxygen evolution conditions: particles versus well-defined extended surfaces. *ACS Energy Lett.* **3**, 2045–2051 (2018).
- Fabbri, E. et al. Developments and perspectives of oxide-based catalysts for the oxygen evolution reaction. *Catal. Sci. Technol.* **4**, 3800–3821 (2014).
- Wohlfahrt-Mehrens, M. & Heitbaum, J. Oxygen evolution on Ru and RuO₂ electrodes studied using isotope labelling and on-line mass spectrometry. *J. Electroanal. Chem.* **237**, 251–260 (1987).
- Binninger, T. et al. Thermodynamic explanation of the universal correlation between oxygen evolution activity and corrosion of oxide catalysts. *Sci. Rep.* **5**, 12167–12172 (2015).
- Grimaud, A. et al. Activating lattice oxygen redox reactions in metal oxides to catalyse oxygen evolution. *Nat. Chem.* **9**, 457–465 (2017).
- Iwakura, C., Hirao, K. & Tamura, H. Anodic evolution of oxygen on ruthenium in acidic solutions. *Electrochim. Acta* **22**, 329–334 (1977).
- Hodnik, N. et al. New insights into corrosion of ruthenium and ruthenium oxide nanoparticles in acidic media. *J. Phys. Chem. C* **119**, 10140–10147 (2015).
- Paoli, E. A. et al. Oxygen evolution on well-characterized mass-selected Ru and RuO₂ nanoparticles. *Chem. Sci.* **6**, 190–196 (2015).
- Rong, X., Parolin, J. & Kolpak, A. M. A fundamental relationship between reaction mechanism and stability in metal oxide catalysts for oxygen evolution. *ACS Catal.* **6**, 1153–1158 (2016).
- Strasser, P. Free electrons to molecular bonds and back: closing the energetic oxygen reduction (ORR)–oxygen evolution (OER) cycle using core–shell nanoelectrocatalysts. *Acc. Chem. Res.* **49**, 2658–2668 (2016).
- Kötz, R. et al. In-situ identification of RuO₄ as the corrosion product during oxygen evolution on ruthenium in acid media. *J. Electroanal. Chem.* **172**, 211–219 (1984).
- AlYami, N. M. et al. Tailoring ruthenium exposure to enhance the performance of fcc platinum@ruthenium core–shell electrocatalysts in the oxygen evolution reaction. *Phys. Chem. Chem. Phys.* **18**, 16169–16178 (2016).
- Cui, C. et al. Compositional segregation in shaped Pt alloy nanoparticles and their structural behaviour during electrocatalysis. *Nat. Mater.* **12**, 765–771 (2013).
- Gan, L. et al. Element-specific anisotropic growth of shaped platinum alloy nanocrystals. *Science* **346**, 1502–1506 (2014).
- Strasser, P. et al. Lattice-strain control of the activity in dealloyed core–shell fuel cell catalysts. *Nat. Chem.* **2**, 454–460 (2010).
- Huang, X. et al. A versatile strategy to the selective synthesis of Cu nanocrystals and the in situ conversion to CuRu nanotubes. *Nanoscale* **5**, 6284–6290 (2013).
- Baletto, F. & Ferrando, R. Structural properties of nanoclusters: energetic, thermodynamic, and kinetic effects. *Rev. Mod. Phys.* **77**, 371–422 (2005).
- Kyriakou, G. et al. Isolated metal atom geometries as a strategy for selective heterogeneous hydrogenations. *Science* **335**, 1209–1212 (2012).
- Alayoglu, S. et al. Ru–Pt core–shell nanoparticles for preferential oxidation of carbon monoxide in hydrogen. *Nat. Mater.* **7**, 333–338 (2008).
- Li, J. et al. Surface evolution of a Pt–Pd–Au electrocatalyst for stable oxygen reduction. *Nat. Energy* **2**, 17111–17119 (2017).
- Denton, A. R. & Ashcroft, N. W. Vegard's law. *Phys. Rev. A* **43**, 3161–3164 (1991).
- Shi, Y. et al. Hot electron of Au nanorods activates the electrocatalysis of hydrogen evolution on MoS₂ nanosheets. *J. Am. Chem. Soc.* **137**, 7365–7370 (2015).
- Nayak, S., McPherson, I. J. & Vincent, K. A. Adsorbed intermediates in oxygen reduction on platinum nanoparticles observed by in situ IR spectroscopy. *Angew. Chem.* **130**, 13037–13040 (2018).
- Stamenkovic, V. R. et al. Improved oxygen reduction activity on Pt₃Ni (111) via increased surface site availability. *Science* **315**, 493–497 (2007).
- Zhang, B. et al. Homogeneously dispersed multimetal oxygen-evolving catalysts. *Science* **352**, 333–337 (2016).
- Suntivich, J. et al. A perovskite oxide optimized for oxygen evolution catalysis from molecular orbital principles. *Science* **334**, 1383–1385 (2011).
- Seitz, L. C. et al. A highly active and stable IrO₂/SrIrO₃ catalyst for the oxygen evolution reaction. *Science* **353**, 1011–1014 (2016).
- Bajdich, M. et al. Theoretical investigation of the activity of cobalt oxides for the electrochemical oxidation of water. *J. Am. Chem. Soc.* **135**, 13521–13530 (2013).
- Kresse, G. & Hafner, J. Ab initio molecular-dynamics simulation of the liquid–metal–amorphous–semiconductor transition in germanium. *Phys. Rev. B* **49**, 14251–14269 (1994).
- Kresse, G. & Furthmüller, J. Efficient iterative schemes for ab initio total-energy calculations using a plane-wave basis set. *Phys. Rev. B* **54**, 11169–11185 (1996).
- Perdew, J. P., Burke, K. & Ernzerhof, M. Generalized gradient approximation made simple. *Phys. Rev. Lett.* **77**, 3865–3868 (1996).
- Kresse, G. & Joubert, D. From ultrasoft pseudopotentials to the projector augmented-wave method. *Phys. Rev. B* **59**, 1758–1775 (1999).
- Monkhorst, H. J. & Pack, J. D. Special points for Brillouin-zone integrations. *Phys. Rev. B* **13**, 5188–5192 (1976).
- Rossmel, J., Logadottir, A. & Nørskov, J. K. Electrolysis of water on (oxidized) metal surfaces. *Chem. Phys.* **319**, 178–184 (2005).
- Rossmel, J. et al. Electrolysis of water on oxide surfaces. *J. Electroanal. Chem.* **607**, 83–89 (2007).
- Man, I. C. et al. Universality in oxygen evolution electrocatalysis on oxide surfaces. *ChemCatChem* **3**, 1159–1165 (2011).
- Gilbert, P. Iterative methods for the three-dimensional reconstruction of an object from projections. *J. Theor. Biol.* **36**, 105–117 (1972).
- Ravel, B. & Newville, M. ATHENA, ARTEMIS, HEPHAESTUS: data analysis for X-ray absorption spectroscopy using IFFFIT. *J. Synchrotron Radiat.* **12**, 537–541 (2005).
- Chen, C. et al. Highly crystalline multimetallic nanoframes with three-dimensional electrocatalytic surfaces. *Science* **343**, 1339–1343 (2014).

Acknowledgements

This work was supported by the National Key R&D Program of China (2017YFA0208300, 2017YFA0700104, 2017YFB0602205 and 2018YFA0208603), the National Natural Science Foundation of China (21522107, 21671180, 91645202, 91421315, 21521091, 21390393 and U1463202) and the Chinese Academy of Sciences (QYZD)-SSW-SLH054). The authors acknowledge funding support from CAS Fujian Institute of Innovation, and thank the photoemission endstations BL1W1B in the Beijing Synchrotron Radiation Facility (BSRF), BL14W1 in the Shanghai Synchrotron Radiation Facility (SSRF) and BL10B and BL11U in the National Synchrotron Radiation Laboratory (NSRL) for help with characterizations.

Author contributions

Y.W. and Y.L. designed the study. Y.Y., X.W., G.W. and W.W. carried out the sample synthesis and electrochemical measurements. K.Z., R.L., W.Y., D.H. and J.L. performed the electron-microscopy characterization. S.H., W.L., Z.H. and C.R. finished the DFT calculations and analysis. W.C., Y.W. and J.D. carried out the in situ and ex situ X-ray absorption fine structure and analysis. Y.C. and B.Z. performed the in situ infrared

experiment. Y.W., Y.Y., S.H. and W.L. wrote the manuscript. The other authors provided reagents and performed some of the experiments. P.S. reviewed the data and revised portions of the manuscript, triggering helpful discussions.

Competing interests

The authors declare no competing interests.

Additional information

Supplementary information is available for this paper at <https://doi.org/10.1038/s41929-019-0246-2>.

Reprints and permissions information is available at www.nature.com/reprints.

Correspondence and requests for materials should be addressed to W.-X.L. or Y.W.

Publisher's note: Springer Nature remains neutral with regard to jurisdictional claims in published maps and institutional affiliations.

© The Author(s), under exclusive licence to Springer Nature Limited 2019